



Spray characteristics of standard and alternative aviation fuels at high ambient pressure conditions

Dongyun Shin^{a,*}, Aman Satija^b, Robert P. Lucht^c

^a School of Aeronautics and Astronautics, Purdue University, 500 Allison Rd, West Lafayette, IN 47906, United States of America

^b School of Mechanical Engineering, Purdue University, 500 Allison Rd, West Lafayette, IN 47906, United States of America

^c School of Mechanical Engineering, School of Aeronautics and Astronautics, Purdue University, 500 Allison Rd, West Lafayette, IN 47906, United States of America

ARTICLE INFO

Keywords:

Alternative aviation fuel
High ambient pressure effect
Hybrid pressure-swirl airblast atomizer
Spray characteristics
Phase Doppler anemometry
Planar laser-induced fluorescence

ABSTRACT

The spray characteristics of standard and alternative aviation fuels generated by a hybrid pressure-swirl airblast (HPSA) atomizer were investigated at high ambient pressure conditions. The measurements were performed in an optically accessible pressure vessel at pressures of 1, 2, 3, 4, 5, and 9.5 bar with heated gas and fuel temperatures of 394 K and 332 K, respectively. The drop size and drop velocity of sprays from a standard (Jet-A) and an alternative (C-5) aviation fuels were measured using phase Doppler anemometry (PDA), and 2-D visualization of spray was imaged using simultaneous fuel-Planar Laser Induced Fluorescence (PLIF) and Mie scattering. The spatially resolved PDA drop size measurements were obtained at 25.4 mm downstream of the swirler exit plane and up to 30 mm in the radial direction from the spray centerline. The Sauter Mean Diameter (D_{32}) was observed to decrease significantly with increasing ambient pressure, up to 5 bar. However, the change in D_{32} was observed to be limited with a further increase in the ambient pressure. A higher swirler pressure drop resulted in a significant reduction in the D_{32} at an ambient pressure of 5 bar. Using simultaneous fuel-PLIF and Mie scattering imaging, the feasibility of the laser sheet drop-sizing (LSD) technique was examined for the spray at high ambient pressure application. In addition, the effect of ambient pressure on the spray cone angle was investigated using both instantaneous and averaged Mie images. The distribution of fuel vapor and droplets in the spray was also imaged and identified by comparing instantaneous fuel-PLIF and Mie images. A phenomenological three-step atomization model was used to predict the drop size and demonstrate the drop size trend with increasing ambient pressure.

1. Introduction

The evaluations of spray characteristics and performance for alternative fuels at realistic gas turbine engine operating conditions are critical tasks as part of the D4054 qualification process for the commercial deployment [1] since combustion performance is strongly affected by atomization quality. When atomization is insufficient, the bulk of liquid or large droplets are produced. This can lead to fuel-rich combustion resulting formation of soot and nitric oxides [2]. On the other hand, sufficient atomization can lead to a greater volumetric heat release rate with a greater surface area due to many fine droplets compared to larger droplets. More vaporization occurs with finer droplets; hence, it is easier to light up and likely to have more complete combustion, resulting in lower pollutant emission [2].

In gas turbine combustors, fuel sprays are injected into highly

turbulent, swirling, and recirculating streams of reacting gases [2]. The pressure and temperature of the ambient gas in the combustor can vary widely depending on engine operability and can strongly affect the fuel atomization. The operating pressure in combustors has been raised continuously in recent years in the quest for better thermal efficiency. Operational pressures can even exceed the critical pressure of the liquid fuel [3]. Higher pressure in the combustor can lead to higher thermal efficiency by improving the specific fuel consumption [3].

Several groups [4–10] have investigated the spray characteristics of prefilming airblast atomizers at elevated ambient pressure and temperature. Batarseh *et al.* [4] and Chrigui *et al.* [6] reported a significant reduction in mean drop size with increasing ambient pressure from 1 to 5 bar, but further increases in ambient pressure resulted in increased D_{32} . The axial velocity of the drop, however, in both studies, was reported to decrease continuously with the ambient pressure. Zheng *et al.*

* Corresponding author.

E-mail address: shin206@purdue.edu (D. Shin).

<https://doi.org/10.1016/j.expthermflusci.2021.110511>

Received 5 May 2021; Received in revised form 7 July 2021; Accepted 17 August 2021

Available online 30 August 2021

0894-1777/© 2021 Elsevier Inc. All rights reserved.

[10] also observed similar trends in mean drop size and axial velocity with increasing ambient pressure, but the variation in drop size was small. Zheng *et al.* [10] attributed this to the counter swirling airblast atomizer in which the atomization process is dominated by the liquid sheet breakup mechanism, which is independent of pressure. In contrast to those findings in the literature [4,6,10], other studies [5,7–9] reported that D_{32} decreased continuously with increasing ambient pressures beyond 10 atm. However, the reduction in D_{32} was observed to diminish with a further increase in the ambient pressure. The different observations on the D_{32} trends with increasing ambient pressure in literature may be caused due to different nozzle geometry and operating conditions used in their studies. In this work, we have used PDA to provide the drop size and drop velocity comparisons at realistic combustor conditions with elevated ambient pressure, up to 9.5 bar, for both standard and alternative aviation fuels using a hybrid pressure-swirl airblast atomizer.

The spray cone angle is a vital combustion parameter since the optimum cone angle can lead to better fuel–air mixing and a wider dispersion of fuel drops within the combustor. Zheng *et al.* [10] reported a widening spray cone angle near the nozzle with increasing ambient pressure from 1 bar to 12 bar; however, the cone angle at locations further downstream of the nozzle remained fairly constant. Besides Zheng *et al.* [10], the studies [4–9] did not provide the effect of ambient pressure on the spray cone angle of the prefilming airblast atomizer. In the present study, the spray cone angle of alternative jet fuel was compared to that of standard fuel using the planar laser sheet imaging technique and investigated to determine the spray fluctuation or contraction at a high ambient pressure environment.

Laser sheet imaging techniques were employed in the present study, fuel-Planar Laser-Induced Fluorescence (fuel-PLIF) and Mie scattering imaging, to obtain simultaneous 2-D images of the spray. PLIF is widely used in spray and combustion applications in which knowledge of the concentration of liquid and vapor phase and 2-D measurements of flame and spray are critical. In PLIF [11], a laser sheet illuminates the flow and excites the ground-state molecules of the fluid to a higher electronic energy state. The excited molecules then de-excite and emit light at a longer wavelength due to a loss of vibrational energy. Depending on the application, a fluorescent dye with an appropriate granularity can be added to the fluid, or an aromatic hydrocarbon that presents naturally in the fuel can be used as a fluorescent dye [11]. Under certain conditions, the population of these tracer species in a unit volume of the fluid is directly proportional to the fluorescence signal [11,12]. This can be used to obtain information regarding the concentration or mass distribution of the spray [12]. Mie scattering is elastically scattered light from particles similar to or larger than the incident light wavelength. Mie scattering provides a 2-D representation of the spray, but only for the liquid phase of the spray, whereas the PLIF signal is detected from both liquid and vapor phases. In the present study, the distribution of the liquid and vapor phases in the spray was determined using both PLIF and Mie scattering images at elevated ambient pressure. Furthermore, the feasibility of the laser sheet drop-sizing (LSD) technique was examined for variable ambient pressure application using both PLIF and Mie images.

In the present study, the spray characteristics of standard and alternative fuels at high ambient pressure conditions were investigated using phase Doppler anemometry (PDA) and fuel-PLIF/Mie imaging. The ambient pressure was set at different values of 1, 2, 3, 4, 5, and 9.5 bar. The fuel temperature, $T_{fuel} = 332$ K, atomizing gas temperature $T_{airbox} = 394$ K, fuel injection pressure $\Delta P_{pilot} = 1.72$ bar, and pressure drop across the gas swirler $\Delta P/P = 3\%$. The spray characteristics considered in this study include the Sauter Mean Diameter (D_{32}), drop axial velocity (U_z), and cone angle (θ) for a standard fuel (A-2) and an alternative fuel (C-5). The same hybrid pressure-swirl airblast (HPSA) atomizer that was used in the previous work [13] was used in this study.

2. Experimental system

2.1. Variable Ambient Pressure Spray test rig

The Purdue Variable Ambient Pressure Spray (VAPS) test rig shown in Fig. 1(a) is capable of creating conditions over a wide range of pressures and temperatures for the ambient gas, atomizing gas, and fuel for spray measurements. The VAPS test rig has two major components: the airbox and the pressure vessel. The airbox is a length of pipe inside the vessel and allows the atomizing gas flow to be isolated from the vessel flow. This creates a pressure difference between the airbox and the pressure vessel. The flow in the airbox exits through the gas swirler of the hybrid pressure-swirl airblast atomizer, which is mounted at the exit of the airbox.

The pressure vessel has four optical windows. The window orientation has been modified and is different than one from the previous study [13]. For the present study, three 127-mm diameter windows are oriented perpendicular to each other, and a 76.2-mm diameter window is oriented at 60° from one of the 127-mm windows as shown in Fig. 1(b). The heated (394 K) nitrogen flow was separated into three lines and supplied directly into the airbox, vessel, and window purge flange. The purpose of the window purge flow was to minimize the fuel wetting on the window by creating an N₂ flow shield near the window surface. These heated flows also prevented condensation on the outer side of the windows. The fuel temperature was measured just upstream of the prime injector inlet port, while the pressure in the pilot fuel line was measured at the inlet of the airbox.

2.2. Hybrid pressure-swirl airblast atomizer

A hybrid pressure-swirl airblast (HPSA) atomizer designed by the Parker-Hannifin Corporation was used in this study. A schematic of the atomizer's internal layout and a Mie scattering image of the resulting spray is shown in Fig. 2. For the results described in this paper, only the pilot circuit was fueled. The atomization process involves: (1) a hollow cone fuel spray exits the pilot nozzle and impinges on the prefilming surface, (2) a fuel film develops along the surface and flows towards the prefilmer tip, (3) ligaments are formed as the fuel film extends from the prefilmer tip, (4) the swirling gas flow disintegrates the ligaments into droplets. Some droplets resulting from primary breakup undergo secondary atomization in the bag breakup regime, resulting in a multiplicity of drop sizes [14]. A detailed discussion of this hybrid atomizer can be found in Mansour *et al.* [15].

2.3. Diagnostic techniques

2.3.1. Planar laser Induced fluorescence and Mie scattering

Simultaneous fuel-PLIF and Mie scattering measurements were performed to provide 2-D visualizations of the spray. In the present work, the aromatics in jet fuel were the species that fluoresced. The fluorescence spectroscopy of kerosene gas (composed of benzene and naphthalene) at high temperature and pressure [16,17] showed that the fluorescence intensity was stronger for 248 nm and 266 nm excitation resulting from a strong absorption of the laser by the aromatics at these wavelengths. Furthermore, the variation in kerosene fluorescence excited by 266 nm wavelength in nitrogen was minimal with ambient pressure at a constant temperature [16]. Therefore, a Q-switched Nd:YAG laser, frequency quadrupled to 266 nm wavelength, was used in the present work for the fuel-PLIF measurements.

Fig. 3 shows the schematic diagram of the PLIF and Mie measurement systems in the VAPS test rig. This excitation light beam profile was expanded to 40 mm in height and collimated into a cylindrical lens to form a sheet, entering the pressure vessel through the fused silica window. The 266-nm pulse energy was approximately 70 mJ/pulse, and the repetition rate was 10 Hz. The fluorescence spectrum of kerosene and 1,2,4 trimethyl benzene are shown in Fig. 4 [16,18]. The A-2 (Jet-A) fuel

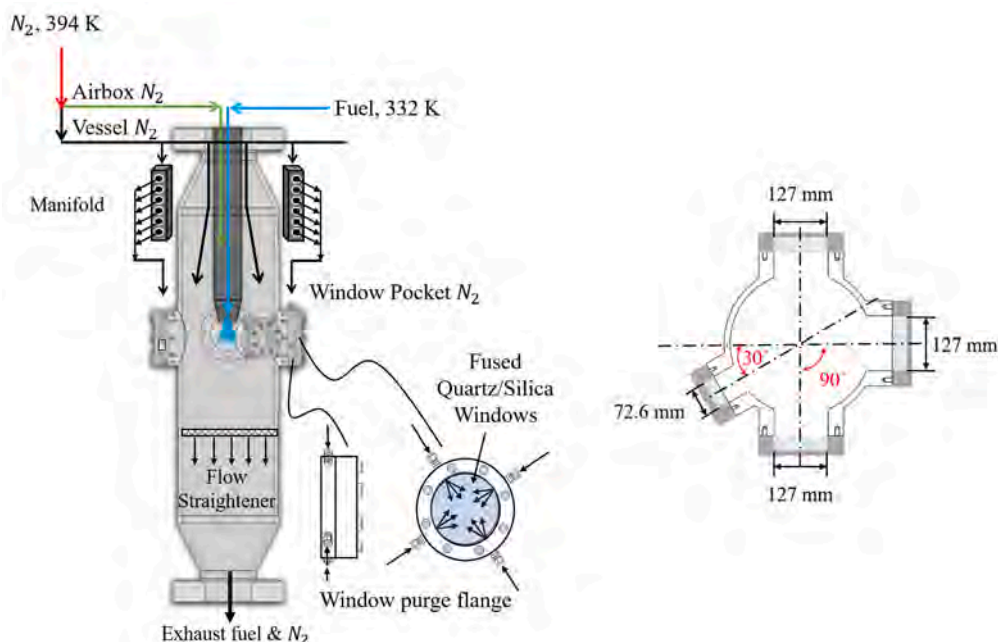


Fig. 1. Schematic diagram of VAPS test rig. (a) Nitrogen and fuel flow lines in the pressure vessel. (b) Orientation of the window ports on the vessel.

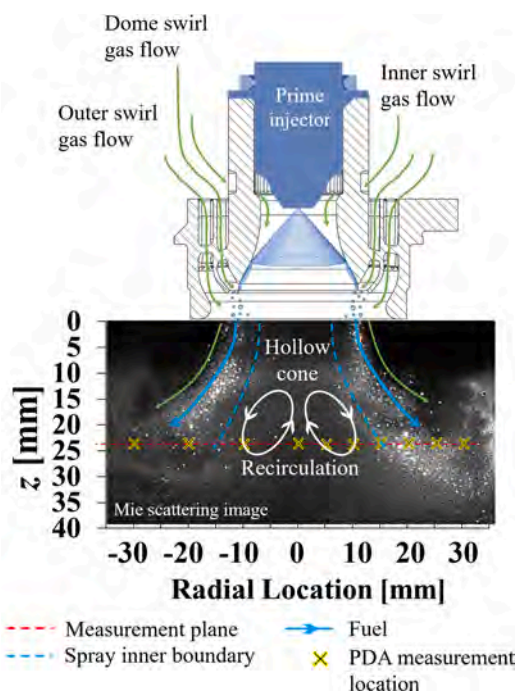


Fig. 2. Schematic diagram of the internal view of the atomizer and the resulting Mie scattering image for the hybrid pressure-swirl airblast atomizer [15]. The measurement plane as a red dashed line is shown along with the location for the pointwise PDA measurements (as yellow crosses). $z = 0$ mm is referenced to the exit plane of the gas swirler. Note that this is modified diagram from one presented by Shin *et al.* [13].

has the same aromatic compounds as kerosene (JP-8), such as alkylbenzene and alkyl-naphthalenes [16,19], while C-5 fuel contains 1,2,4-trimethylbenzene as its aromatic compounds [19]. The fuel fluorescence and Mie-scattered light were separated using a dichroic beam splitter, which reflected the 266-nm Mie-scattered light and transmitted the fluorescence above 266 nm. Two time-synchronized ICCD cameras (PI-MAX4) equipped with UV lenses (Nikkor 70 ~ 210 mm f/4.5 and

Objectif UV 100f/4.5) captured the scattered light and fluorescence from fuel. For the PLIF camera, a transmission filter centered at 320 nm with a bandpass of 40 nm was used to capture the fluorescence spectra. This scheme captures the entire emission range for Jet-A and almost half of the fluorescence range for C-5 fuel. Although some fluorescence at 270 nm transmitted through the 266 nm bandpass filter, for the Mie signal camera, that contribution of fluorescence signal was negligibly small.

2.3.2. Phase Doppler anemometry

A phase Doppler anemometry (PDA) system was used to measure the droplet diameter and droplet velocity. The phase difference of Doppler-burst signals from different detectors determines the droplet diameter, while the frequency of Doppler-bursts determines the droplet velocity. The fundamentals of the PDA measurement system can be found in references such as Albrecht *et al.* [20]. The layout of the PDA system around the VAPS test rig is shown in Fig. 5. The PDA system was used previously for the LBO, and engine cold start measurements [13,21], except the scattering angle was different. The scattering angle was set to 30° in this study, which is a recommended angle from PDA system manufacturer due to a strong forward scattering. In the previous studies [13,21], this scattering angle was limited to 60° due to the window orientation prior to modification. Measurements were performed at radial locations between ± 30 mm from the spray center line in increments of 5 mm. The measurement region of the PDA system was constrained to a range of 60 mm due to interference from the mounting flange of the 76.2 mm diameter window. Ten measurements, each with 20,000 samples, were recorded at each radial location (r) per test condition. The velocity validation and spherical validation rates were in the range of 95 ~ 97 % and 88 ~ 95%, respectively. The key optical settings for the PDA measurement are shown in Table 1. The average uncertainties of the PDA measurements for all ambient pressure conditions are listed in Table 2. The uncertainty value at each ambient pressure condition were obtained using the standard deviations of ten repeated measurements at each radial location.

The measured D_{32} values at several radial locations for $z = 25.4$ mm were used to calculate a single value of line-of-sight drop size (D_{32o}) that measurement plane. The line-of-sight D_{32} is the averaged D_{32} over the radial profile of the spray and is weighted by the measured volume flux

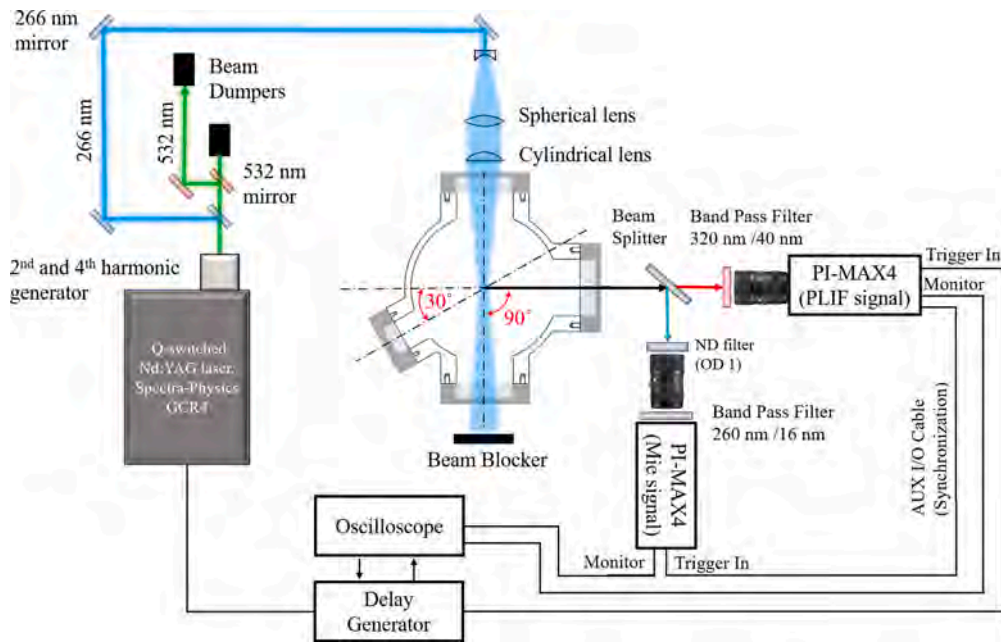


Fig. 3. Schematic diagram of the fuel-PLIF and Mie measurement system in the VAPS rig.

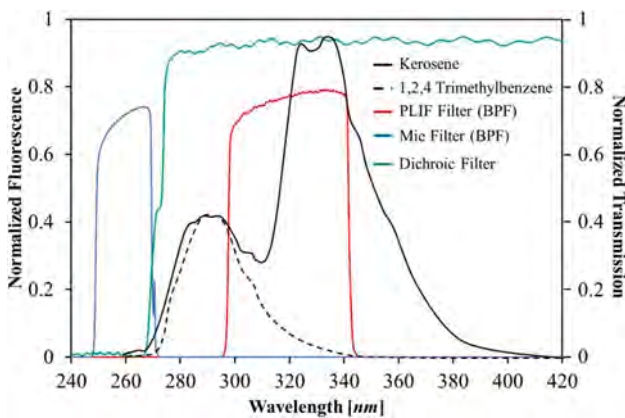


Fig. 4. Emission wavelength of fuels with 266 nm excitation wavelength [16,18] and optical filters configuration.

at each radial location. Similar to the approach by Dodge *et al.* [22], the line-of-sight drop size (D_{32o}) can be obtained via:

$$D_{32o} = \frac{\sum_1^n D_{32}(r)q(r)}{\sum q(r)} \quad (1)$$

Here, r is the radial location from the spray center, and n is the number of radial locations. $D_{32}(r)$ and $q(r)$ are the measured D_{32} and the volume flux of droplets in axial direction through the probe volume ($\text{cm}^3/\text{cm}^2/\text{s}$) at each radial location, respectively. The PDA system provides a local fuel volume flux at each measurement point by measuring the number of droplets passing through the probe volume. This line-of-sight drop size was used to demonstrate the effect of ambient pressure on the spray structure for each fuel and compared to the model prediction.

2.4. Test conditions

The high ambient pressure conditions were defined here as following: vessel pressure $P_{vessel} = 1, 2, 3, 4, 5, 9.5$ bar, fuel temperature $T_{fuel} = 332$ K, atomizing gas temperature T_{airbox} of 394 K, and fuel injection pressure $\Delta P_{pilot} = 1.72$ bar, and the pressure drop across the gas

Table 1
Optical settings for PDA system.

Aperture mask	Mask A
Spatial filter	Slit 200 μm
Scattering angle	30°
Receiver optic lens	f 310 mm
Transmitter optic lens	f 400 mm

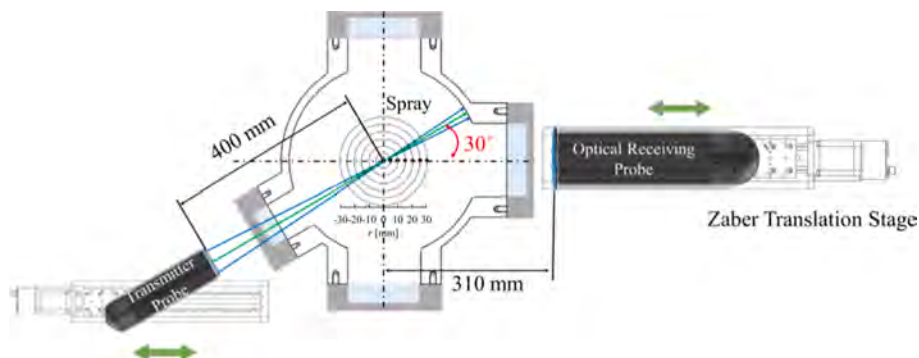


Fig. 5. Schematic diagram of the PDA system and its geometry relative to the VAPS rig.

Table 2
Averaged uncertainties for PDA measurements for A-2 fuel.

r [mm]	$U(D_{32})$	$U(U_z)$
30	1.6 %	1.2 %
25	1.4 %	0.7 %
20	1.4 %	2.3 %
15	1.5 %	4.2 %
10	2.7 %	4.0 %
5	2.8 %	2.2 %
0	3.6 %	1.2 %

swirler $\Delta P/P = 3\%$. The fuel injection pressure is defined as the pressure differential between the fuel line and the vessel. At $\Delta P_{pilot} = 1.72$ bar, the mass flow rate measured by the Coriolis flowmeter was 2.52 g/s. The pressure drop across the gas swirler is the pressure difference between the airbox and the vessel. At $\Delta P/P = 3\%$, the calculated gas velocity at the exit of the swirler was 82 m/s, which was considered to be an incompressible flow. The axial distance (z) downstream from the swirler exit plane was set at 25.4 mm for the PDA measurements. The uncertainty of each operating parameter is shown in Table 3, following the approach of Kline et al. [23].

3. Test fuels

Jet-A (A-2) and C-5 were investigated in this study. The standard aviation fuels are represented by code A while the alternative fuels are represented by code C [1]. The A-2 fuel was found to be a “nominal fuel” based on three combustion-related properties: flash point, viscosity, and aromatics content [1]. The C-5 fuel was created by blending 1,3,5 trimethyl benzene with a C10 isoparaffinic solvent. This test fuel has an extremely flat boiling range at roughly 165 °C and was designed to evaluate the impact of a very limited vaporization range of the fuel on the combustor [1]. Detailed discussions regarding physical properties, chemical compositions, and fuel selection methods can be found in Edward et al. [19].

Table 4. shows the key physical properties of each fuel, such as surface tension, viscosity, and density. These properties were extrapolated from a fuel temperature of 328 K using measured values provided by the Air Force Research Laboratory (AFRL) [19]. The viscosity, surface tension, and density values of the C-5 fuel were found to be different from A2 by -53% , -15% , and -4.7% , respectively.

4. Results and discussion

4.1. Effect of ambient pressure on drop diameter and drop velocity

The spray characteristics of the standard (A-2) and alternative (C-5) fuels were investigated using the Sauter Mean Diameter (D_{32}) and drop mean axial velocity (U_z). The symmetrical nature of the spray properties was consistently observed for both fuels, and therefore only half of the spray data obtained from the PDA measurements are presented. Fig. 6 shows the trends of D_{32} and U_z at $P_{vessel} = 1, 2, 3, 4, 5,$ and 9.5 bar for the baseline condition corresponding to $\Delta P/P = 3\%$, $\Delta P_{pilot} = 1.72$ bar, $T_{fuel} = 332$ K, and $T_{airbox} = 394$ K at $z = 25.4$ mm. As reported in the previous studies [13,21], the spray generated from the hybrid pressure-swirl

Table 3
Uncertainty of operating parameters.

Operating Parameters	Operating Conditions	Uncertainty
P_{vessel}	1, 2, 3, 4, 5, 9.5 bar	0.4 %
ΔP_{pilot}	1.72 bar	2.5 %
$\Delta P/P$	3 %	2.8 %
T_{fuel}	332 K	4.2 %
T_{airbox}	394 K	1.1 %
m_{fuel}	2.52 g/s	2.5 %

Table 4

Fuel physical properties at 332 K. The data points were extrapolated using measured values provided by AFRL [19].

Fuel Type	Temp.	μ [kg/m·s]	σ [N/m]	ρ [kg/m ³]	Notable Characteristics
A-2	332 K	9.2E-04	0.023	770	Average flash point, viscosity, aromatics
C-5	332 K	4.4E-04	0.020	734	Flat boiling range (boils at 165 °C)

airblast atomizer in this study was a hollow-cone spray.

The effect of ambient pressure (P_{vessel}) was found to affect the mean drop size significantly. As shown in Fig. 6, a significant decrease in D_{32} was observed with increased ambient pressure from 1 bar to 2 bar. The D_{32} continued to decrease gradually with further increases in the ambient pressure from 2 bar to 9.5 bar. However, the effect of ambient pressure on drop diameters diminished with further increase in ambient pressure, and a minimal decrease in D_{32} value was observed when the ambient pressure increased from 5 bar and 9.5 bar. Furthermore, the variation in drop diameter at each radial location became smaller as the ambient pressure increased. Due to higher gas density, the greater inertial force on the liquid sheet or ligament promoted greater disturbance on the liquid sheet or ligament. Hence, this resulted in smaller droplets [24]. The drop axial velocity was observed to be similar for all ambient pressures, as shown in Fig. 6(b) and (d). This is believed to be attributed to the smaller droplets that responded quickly to the gas flow and followed closely the gas streamline. This atomizing gas velocity was kept the same for all ambient pressure cases by maintaining constant pressure drop. Since the reported drop velocity values are the averaged velocities of all 20,000 droplets acquired at each radial location, they are heavily weighted towards the velocities of those smaller droplets. However, more experimental work, such as time-resolved PIV measurement of the surrounding gas field, would be necessary to provide a clear explanation on this drop velocity trend. Droplets near the spray edge were observed to slow down with increasing pressure as they are more affected by the drag force. The recirculation zone at $z = 25.4$ mm can be defined approximately within $r = \pm 12$ mm in the spray since the negative drop velocity values within $r = \pm 12$ mm indicate that droplets are traveling towards the nozzle. From Fig. 6(b) and (d), it can also be seen that the radial location of 12 mm (approximately) is the transition point where those negative drop velocity values become positive values, indicating the droplets are traveling downward from the nozzle. This hollow-cone region boundary was observed to be preserved at higher ambient pressure. The uncertainty bars shown in Fig. 6(b) and (d) indicate the root-mean-squared (RMS) for the axial velocity.

The drop size probability density functions (PDFs) and cumulative density functions (CDFs) are shown in Fig. 7 for C-5 fuel at radial locations of 0 and 20 mm. Each radial location is indicated as a red box in the spray image. The PDFs and CDFs at both radial locations were observed to shift towards the smaller drop diameter range with increasing ambient pressure. The number of smaller drop diameters at both radial locations increased with increasing P_{vessel} while the number of larger drop diameters decreased at higher P_{vessel} . This observation supports the trend of decreasing in D_{32} with increasing P_{vessel} . Moreover, it can be seen that a greater number of smaller droplets present at the spray center ($r = 0$ mm) compared to those numbers near the spray edge ($r = 20$ mm).

Fig. 8 shows the effect of swirler pressure drop ($\Delta P/P$) on D_{32} and U_z at $P_{vessel} = 5$ bar for A-2 fuel. The pressure drop was varied to values of 2, 3, and 6 % at $\Delta P_{pilot} = 1.72$ bar, $T_{fuel} = 332$ K, $T_{airbox} = 394$ K, and $z = 25.4$ mm. As shown in Fig. 8(a), the D_{32} decreased with increasing $\Delta P/P$ and tend to be monodisperse across the radial locations at higher $\Delta P/P$. The drop axial velocity was observed to increase with increasing $\Delta P/P$ as shown in Fig. 8(b). Greater inertial force of the gas flow with increasing $\Delta P/P$ is attributed to form smaller droplets.

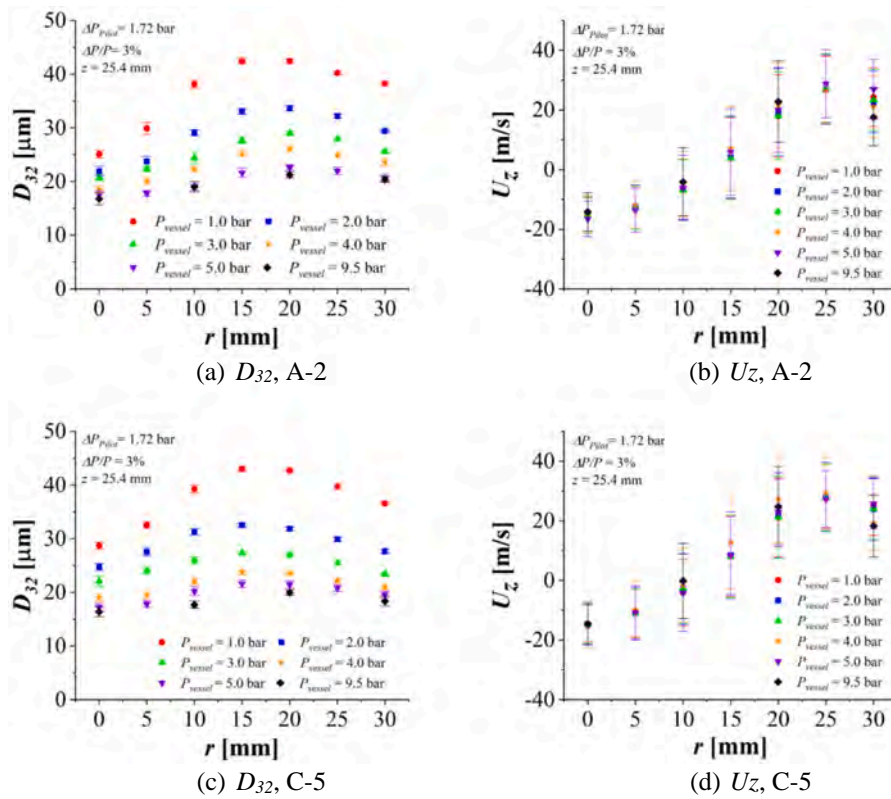


Fig. 6. Comparisons of drop diameters and drop velocities for A-2 and C-5 fuels at $P_{vessel} = 1, 2, 3, 4, 5,$ and 9.5 bar, $\Delta P/P = 3\%$, $\Delta P_{pilot} = 1.72$ bar, $T_{fuel} = 332$ K, and $T_{airbox} = 394$ K for $z = 25.4$ mm.

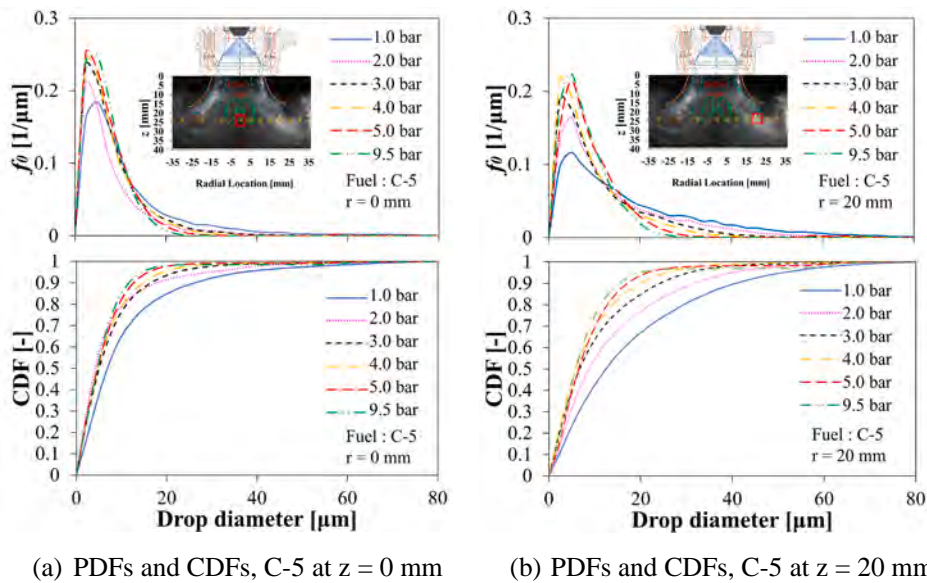


Fig. 7. Comparison of number probability density functions and cumulative density function for C-5 fuel at $P_{vessel} = 1, 2, 3, 4, 5,$ and 9.5 bar, $\Delta P/P = 3\%$, $\Delta P_{pilot} = 1.72$ bar, $T_{fuel} = 332$ K, $T_{airbox} = 394$ K, and $r = 0$ and 20 mm for $z = 25.4$ mm.

4.2. Laser sheet spray measurement

Fuel-PLIF and Mie scattering images were acquired at 5 Hz for both A-2 and C-5 fuels at $P_{vessel} = 1, 2, 5,$ and 9.5 bar, $\Delta P/P = 3\%$, $\Delta P_{pilot} = 1.72$ bar, $T_{fuel} = 332$ K, and $T_{airbox} = 394$ K. Fig. 9 shows normalized instantaneous and averaged PLIF and Mie images at $P_{vessel} = 2$ and 9.5 bar for A-2 fuel. 200 images were used to create an averaged image. From the instantaneous images shown in Fig. 9(a), more droplets were

observed in the hollow cone region at higher ambient pressure. This is attributed to an increase in the number of smaller droplets at higher ambient pressure, as also observed in PDA measurements. These smaller droplets tend to recirculate into the hollow-cone region. This increase in the number of smaller droplets causes a greater number of scattering and absorption/emission events. Moreover, the probability of the reabsorption event will decrease for smaller droplets. Therefore, both PLIF and Mie signals were observed to be increased at higher ambient

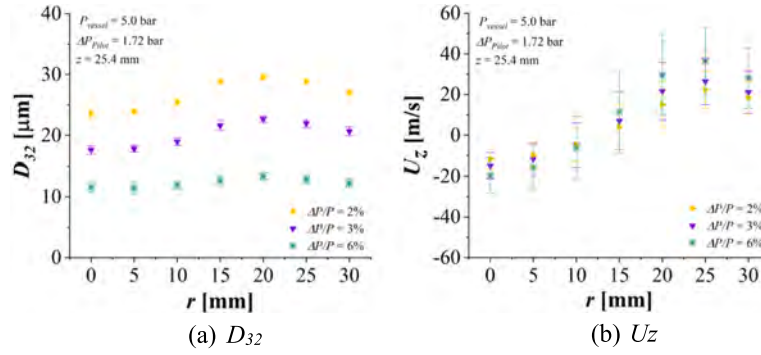


Fig. 8. Comparisons of drop diameters and drop velocities for A-2 fuel at $\Delta P/P = 2, 3,$ and 6% , $P_{vessel} = 5$ bar, $\Delta P_{pilot} = 1.72$ bar, $T_{fuel} = 332$ K, and $T_{airbox} = 394$ K for $z = 25.4$ mm.

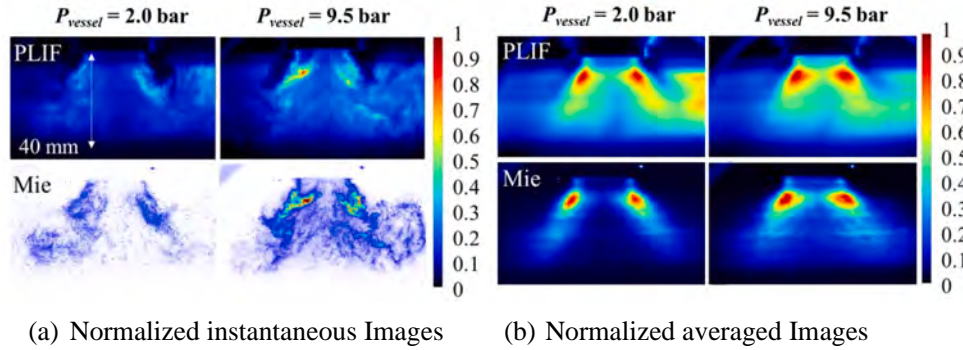


Fig. 9. Instantaneous and averaged PLIF and Mie images at $P_{vessel} = 2.0$ and 9.5 bar, $\Delta P/P = 3\%$, $\Delta P_{pilot} = 1.72$ bar, $T_{fuel} = 332$ K, and $T_{airbox} = 394$ K for A-2 fuel.

pressure. The averaged PLIF and Mie images from Fig. 9(b) also show that the signals in the hollow-cone region increased with ambient pressure.

4.2.1. Feasibility of the laser sheet drop-sizing technique at high ambient pressure application

Using simultaneous fuel-PLIF and Mie images, the laser sheet drop-sizing (LSD) technique was performed to obtain the D_{32} map of the spray, which is a unique feature compared to a point-wise measurement such as a PDA system. The LSD technique is based on the assumption that the fluorescent light signal from the droplet, $I_f(D)$, is proportional to the volume of the droplet ($i.e. I_f(D) = \frac{1}{a_f} D^3$) while the scattered light signal from the droplet, $I_s(D)$, is proportional to the surface area ($i.e. I_s(D) = \frac{1}{a_s} D^2$) [25–28]. Parameter D is the drop size, and a_s and a_f are the unique constants to each experimental setup, such as the camera sensitivity, collection efficiency of the optics, laser sheet intensity, etc. [25]. With this signal-droplet proportionality assumption, the LIF and Mie signal ratio can then represent the D_{32} , as shown in Eq. (2) [25].

$$D_{32} = \frac{\int_{D=0}^{\infty} D^3 dN(D)}{\int_{D=0}^{\infty} D^2 dN(D)} = \frac{\int_{D=0}^{\infty} \frac{1}{a_f} I_f(D) dN(D)}{\int_{D=0}^{\infty} \frac{1}{a_s} I_s(D) dN(D)} = \frac{1}{K} \frac{\int_{D=0}^{\infty} I_f(D) dN(D)}{\int_{D=0}^{\infty} I_s(D) dN(D)}, \quad \text{where } K = \frac{a_f}{a_s} \quad (2)$$

Here, dN is the number of droplets within the drop size class (D). Parameter K is the calibration factor that is related to the LIF/Mie signal ratio to the D_{32} of the measured droplets. Although the LSD technique has been applied in various spray characterization studies [7,29–33], it has not been applied or validated for the spray at variable ambient pressure conditions. In this section, the feasibility of the LSD technique for the spray at high ambient pressure application was examined.

Fig. 10 shows the D_{32} estimation results using the laser sheet drop-sizing (LSD) technique [26–28]. Laser absorption and laser sheet corrections were not required since the PLIF, and the Mie scattering images were obtained simultaneously on identical ICCD cameras. In order to match the field of views, a cross-correlation was performed between the instantaneous PLIF and Mie images by identifying the pixel locations of the observable droplets on both images. Averages of 200 PLIF and 200 Mie images were overlapped to obtain the ratio of LIF and Mie signals. The signal dependence on the laser spatial profile was canceled by the ratio. The D_{32} map estimation using a ratioed LIF and Mie signals are shown in Fig. 10(a) and (b) for $P_{vessel} = 1$ and 2 bar cases [29,31,34].

The LIF/Mie signal ratio and the measured drop sizes by PDA system at $z = 25.4$ mm were used for the drop size calibration for the case of $P_{vessel} = 1$ bar, as shown in Fig. 10(a). This calibration was used to generate the estimated D_{32} map. For validation, the estimated D_{32} values at the measurement location (white dot) for $z = 12.7$ mm were compared to measured D_{32} values at that same measurement locations. In the present work, the LIF and Mie signals were not found to be proportional to the volume (D^3) and surface area (D^2) of the droplet. Therefore, the calibration curve shown in Fig. 10(a) was found to be not following the typical trend of increasing LIF/Mie ratio with increasing drop size [7,31–33], but showed an opposite trend. This is attributed to multiple scattering [35,36] and high aromatic concentration in the fuel [37–39]. Multiple scattering is a phenomenon in which a Mie photon scatters off several other droplets before reaching the CCD/ICCD camera sensor. These multiple scattering paths of photons can lead to a misinterpretation of the droplet size. In addition, the photons may not reach the camera sensor due to multiple scattering [39]. This leads to a loss in the Mie signal. The LIF signal may be absorbed or scattered by intervening droplets or vapor phase. A high concentration of aromatic or fluorescent dye in the liquid will increase the re-absorption within the droplet and deviate the LIF signal's proportionality to D^3 [37,40].

It was also discovered that the drop size calibration obtained from

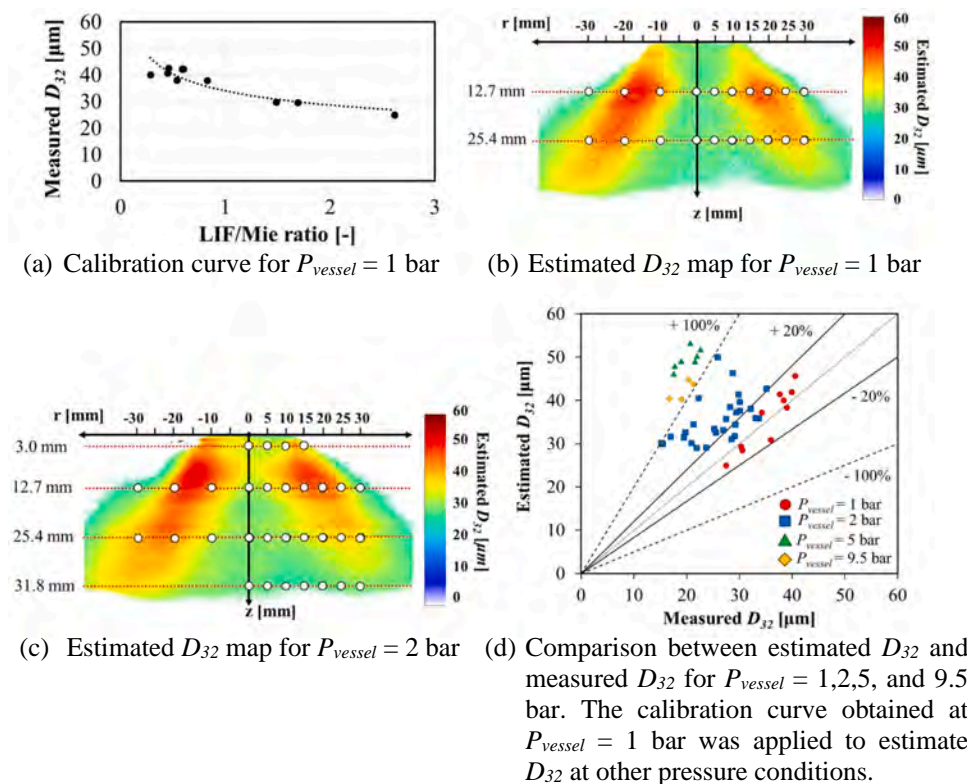


Fig. 10. D_{32} estimation result using LSD technique for $P_{vessel} = 1, 2, 5,$ and 9.5 bar.

one ambient pressure condition was not applicable to any other ambient pressure conditions. The calibration curve obtained at $P_{vessel} = 1$ bar, as shown in Fig. 10(a), was used to calculate D_{32} values on the spray map for other ambient pressure conditions. For example, Fig. 10(c) shows the estimated D_{32} map for $P_{vessel} = 2$ bar using the calibration from Fig. 10(a). These estimated D_{32} values at the measurement locations (white dots) were compared to the measured D_{32} values at the same measurement locations, as shown in Fig. 10(d). The percentage of deviation from the measured D_{32} was observed to increase significantly for other pressure conditions. A LIF/Mie ratio value should be assigned for each PDA measurement point. However, it was observed that two different measured D_{32} values were found for an identical LIF/Mie ratio value. Furthermore, the calibration between LIF/Mie ratio and measured D_{32} for each ambient pressure condition was found to be significantly different. It is believed to be because the scattering signal scales with the number density of particles [41]. As shown in Fig. 7, the number of smaller droplets increased with increasing ambient pressure at a constant fuel flow rate, resulting in increased total number of droplets. Thus, both LIF and Mie signals were scaled differently at each ambient pressure, resulting in different calibration factors for each ambient pressure case.

Therefore, the Structured Light Illumination Planar Imaging (SLIPI) technique is suggested to suppress the multiple scattering effectively in LSD measurement for more accuracy [30,32,33]. Furthermore, it is suggested to use a fluorescence dye to control its concentration in LIF measurement with appropriate excitation laser wavelength, which does not excite any of aromatic contents in the fuel, rather than relying on the aromatic content present in the fuel [37,40].

4.3. Effect of ambient pressure on cone angle

The full cone angle was estimated using both 200 instantaneous Mie images and averaged Mie images at each ambient pressure condition. As shown in Fig. 11(a), the spray boundaries in each instantaneous image were defined using the Canny edge detection method [42]. A threshold

was set to include most of the droplet clusters in the outer spray boundaries for each ambient pressure condition. The angle between two lines along the outer spray boundaries was estimated as a full spray cone angle. Fig. 11 (b) provides the estimation of full cone angle (2θ) at $P_{vessel} = 1, 2, 5,$ and 9.5 bar near $z = 6.0, 18.0,$ and 25.4 mm for A-2 and C-5 fuels. The solid and dashed lines indicate the linear trends of cone angle measurements at each ambient pressure for A-2 and C-5 fuels, respectively.

The cone angle estimation shows that the effect of ambient pressure on the spray cone angle at $r = 6.0$ and 25.4 mm was minimal for both fuels. The fluctuations of the cone angle near $z = 6.0$ mm and 25.4 mm were observed to be similar, and those values were found to be ± 8 and ± 9 respectively for both A-2 and C-5 fuels. The values for angle fluctuation are the standard deviation of estimated spray cone angles from 200 instantaneous images at each pressure condition. The cone angle estimated at $z = 18.0$ mm, however, was observed to increase with increasing ambient pressure. This is attributed to the entrainment of smaller droplets at higher ambient pressure. Since smaller droplets tend to respond quickly to the gas flow due to their smaller inertia, these small droplets were entrained by the gas flow and recirculated outwardly. This entrainment phenomenon is well captured in Fig. 12(c), (f), and (i) in Fuel Liquid/Vapor Distribution section.

4.4. Fuel liquid/vapor distribution

The liquid and vapor discrimination analysis was performed using the PLIF and Mie images. Fig. 12 shows pairs of simultaneously captured PLIF (left) and Mie (middle) images and the normalized difference image from PLIF and Mie images (right) at $P_{vessel} = 1, 2,$ and 9.5 bar. Both PLIF and Mie images were divided by the peak intensity value. The differences of images were calculated by subtracting the Mie image from the PLIF image. The linear normalization was done on the difference image to obtain the normalized difference image on a scale of 0 to 1, as shown in Fig. 12(c), (f), and (i).

In this comparison, it should be noted some factors affect the PLIF

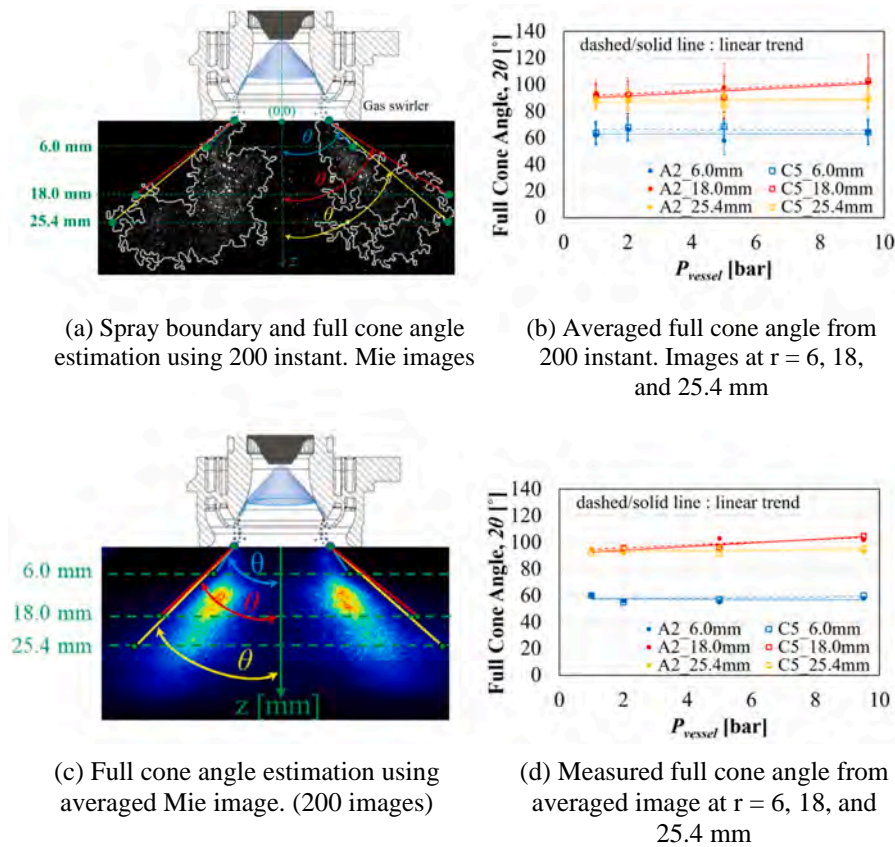


Fig. 11. Full cone angle estimations for A-2 and C-5 fuels at $P_{vessel} = 1$ bar, $\Delta P/P = 3\%$, $\Delta P_{pilot} = 1.72$ bar, $T_{fuel} = 332$ K, and $T_{airbox} = 394$ K. Blue color indicates $z = 6.0$ mm. Red color indicates $z = 18.0$ mm. Yellow color indicates $z = 25.4$ mm.

and Mie signals differently. Ideally, the Mie scattered light signal is proportional to the surface area of the droplets, whereas the LIF signal is proportional to the volume of the droplets [28]. However, this hypothesis was not valid in the present work, as also demonstrated in other studies [25,37,40,43]. This will influence the LIF and Mie light signals differently where the droplets have different sizes depending on location in the spray. Another factor to consider is the multiple scattering, so-called diffuse scattering, within the spray [44]. Diffuse scattering from droplets on the periphery of the spray can be absorbed by the droplets near the centerline and converted to fluorescence. The presence of signal inside of the hollow cone region in the spray, as shown in Fig. 12(a), (d), and (g), is likely caused by diffuse scattering from near the laser sheet plane [35,36]. Thus, the comparison between the Mie and LIF images presented in this section is non-quantitative. However, it can be a useful approach to identify and distinguish liquid and vapor region in the spray.

From Fig. 12(b), (e), and (h), it is evident that the number of droplets near the spray center increased at higher ambient pressure. This is believed to be due to an increased number of smaller droplets at higher ambient pressure, as observed from droplet PDF comparison in Fig. 7. Fig. 13 shows the data rate of PDA measurements at each radial location for the C-5 fuel. The PDA data rate near the center of the spray increases significantly with increasing ambient pressure. This observation supports the hypothesis that a significant number of smaller droplets are recirculated into the hollow cone region and also increase the number of scattering events and signals by increasing the surface area (D^2) [45]. Smaller droplets at $P_{vessel} = 9.5$ bar were observed to have more tendency of following the gas flow compared to those observed at lower P_{vessel} , as shown in Fig. 12(c), (f), and (i). This observation supports the increase in spray cone angle at $z = 18$ mm with increasing ambient pressure due to the entrainment of smaller droplets.

5. Semi-empirical model

A semi-empirical model for the hybrid pressure-swirl airblast (HPSA) atomizer spray was developed in a previous study by Shin et al. [21]. Although the model developed in the previous study was able to predict the drop size trend with increasing ambient pressure, the discrepancy between the predicted and measured drop size values was significant, especially at higher ambient pressure. This is believed to be due to the fact that the previous model did not consider the variation of the pressure-swirl spray cone angle with increasing ambient pressure in the calculation. The contraction of the pressure-swirl spray at elevated ambient pressure has been generally observed by other studies [2,24,46]. This contraction in the cone angle reduces the length of film development on the prefilming surface (r) and may affect the film thickness on the surface. Moreover, the pressure-swirl spray may interact directly with the atomizing gas from dome/outer swirlers without impingement due to the smaller cone angle.

The model used in this work calculates the pressure-swirl spray cone angle variation as a function of ambient gas density by implementing the correlation provided by Dodge and Biaglow [47], whereas the previous model predicted the cone angle as a function of pilot nozzle geometry. This implementation improved the model in predicting the drop size trend with less discrepancy between the predicted and measured drop size value at higher ambient pressure. Detailed methodology of the model can be found in Shin et al. [21]. The phenomenological atomization process considered in this semi-empirical model can be summarized as follows:

- (1) the pressure-swirl spray generated from the pilot nozzle breaks into drops as it penetrates both axial and radial directions and drops impinge on the prefilming surface.

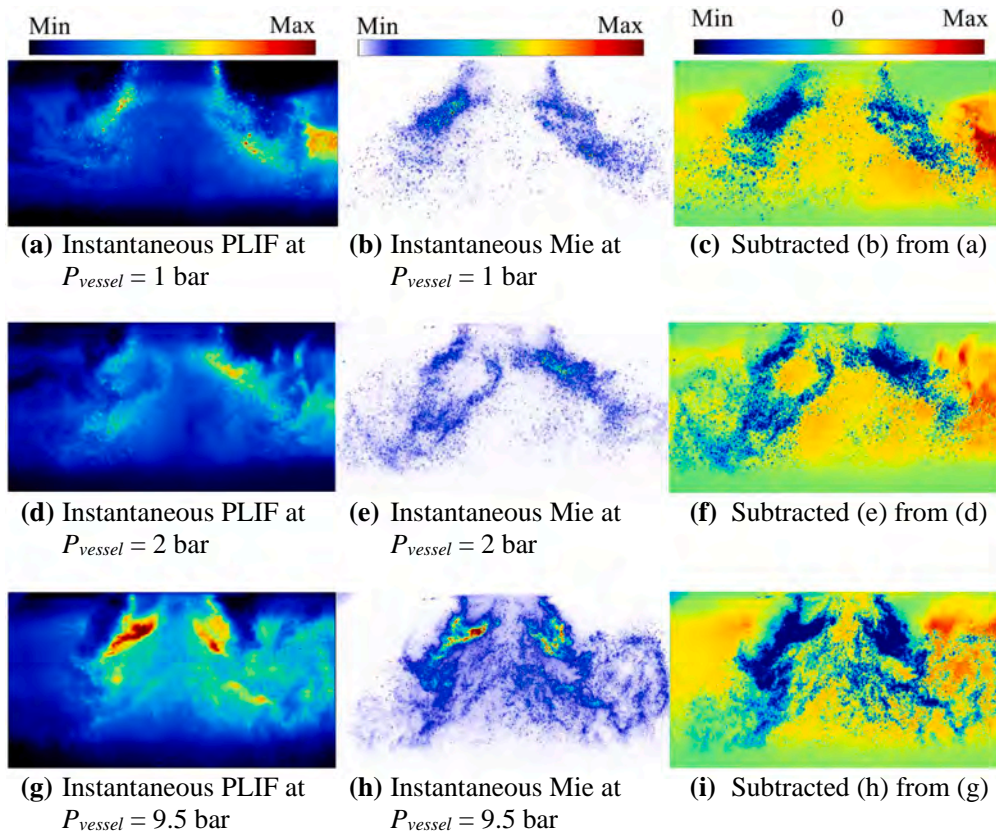


Fig. 12. Liquid – vapor discrimination A-2 fuel at $P_{vessel} = 1, 2,$ and 9.5 bar, $\Delta P/P = 3\%$, $\Delta P_{pilot} = 1.72$ bar, $T_{fuel} = 332$ K, and $T_{airbox} = 394$ K.

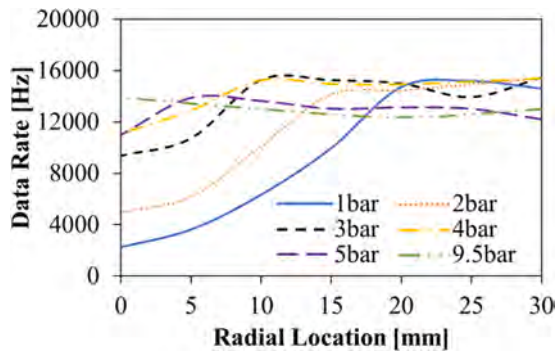


Fig. 13. Comparison of data rate measurement from PDA at each ambient pressure for C-5 fuel.

- (2) the impinged droplets then form a fuel film on the surface and flow towards the prefilmer tip along with the inner swirl gas flow.
- (3) the fuel film tears into ligaments as it extends from the prefilmer tip.
- (4) ligaments then interact with the outer swirling gas flow and are disintegrated into droplets.

The model captures the atomization process through three different sub-models: pressure-swirl spray drop formation, drop impingement and film formation, and aerodynamic breakup [21]. Fig. 14 shows the schematic diagram of the atomization process of the hybrid pressure-swirl airblast atomizer. Location A corresponds to the pressure-swirl spray drop formation sub-model adopting the linear sheet instability analysis by Senecal *et al.* [48]. This is the location where the initial sheet thickness, sheet breakup length, cone angle, sheet thickness at the breakup, and pressure-swirl spray droplet size are determined. Location

B corresponds to the droplet impingement and film formation sub-model. In this location, the film thickness and velocity resulted from the droplet impingement on the prefilming surface are determined by adopting an impinging jet model by Naber *et al.* [49] and Ibrahim *et al.* [50]. Location C corresponds to the aerodynamic breakup sub-model. This is the location where the ligament diameter, ligament length, and final droplet size resulted from the ligament breakup by the atomizing gas are determined.

The predicted final drop size (d_D) can be expressed as [21]

$$d_D = \frac{12}{\left(1 + \frac{1}{ALR}\right)^{-1} \left(C \frac{U_g^2 \rho_L}{\sigma}\right) + 4 \left(\frac{2}{d_L} + \frac{1}{\lambda_L}\right)}, \quad \text{where } C = \frac{a'}{ALR^{b'} U_g^{c'}} \quad (3)$$

Here, ALR is the air-to-liquid ratio, and U_g is the atomizing gas velocity. σ and ρ_L indicate liquid–gas surface tension and liquid density, respectively. The parameters d_L and λ_L are the ligament diameter and the ligament length. Adopting similar energy considerations, as discussed in Lefebvre [51], this semi-empirical model was derived based on the assumption that the energy required to atomize a ligament is equal to some fraction of the kinetic energy of the atomizing gas. The first term in the denominator accounts for the effect of aerodynamic forces on the drop size, and the second term considers the liquid physical properties.

The parameter C is related to the energy transfer efficiency of the atomizing gas to the liquid [51–53]. In this work, the parameter C is correlated to ALR and U_g . It is hypothesized that the parameter C decreases with increasing U_g . As the velocity of the atomizing gas increases, the local static pressure decreases, which causes the low-velocity surrounding gas to be entrained into the atomizing gas stream and to be accelerated [53]. This resulted in reducing the kinetic energy available for atomization. The parameter C also decreases with increasing ALR. At higher ALR, the rate of radial expansion of the exiting

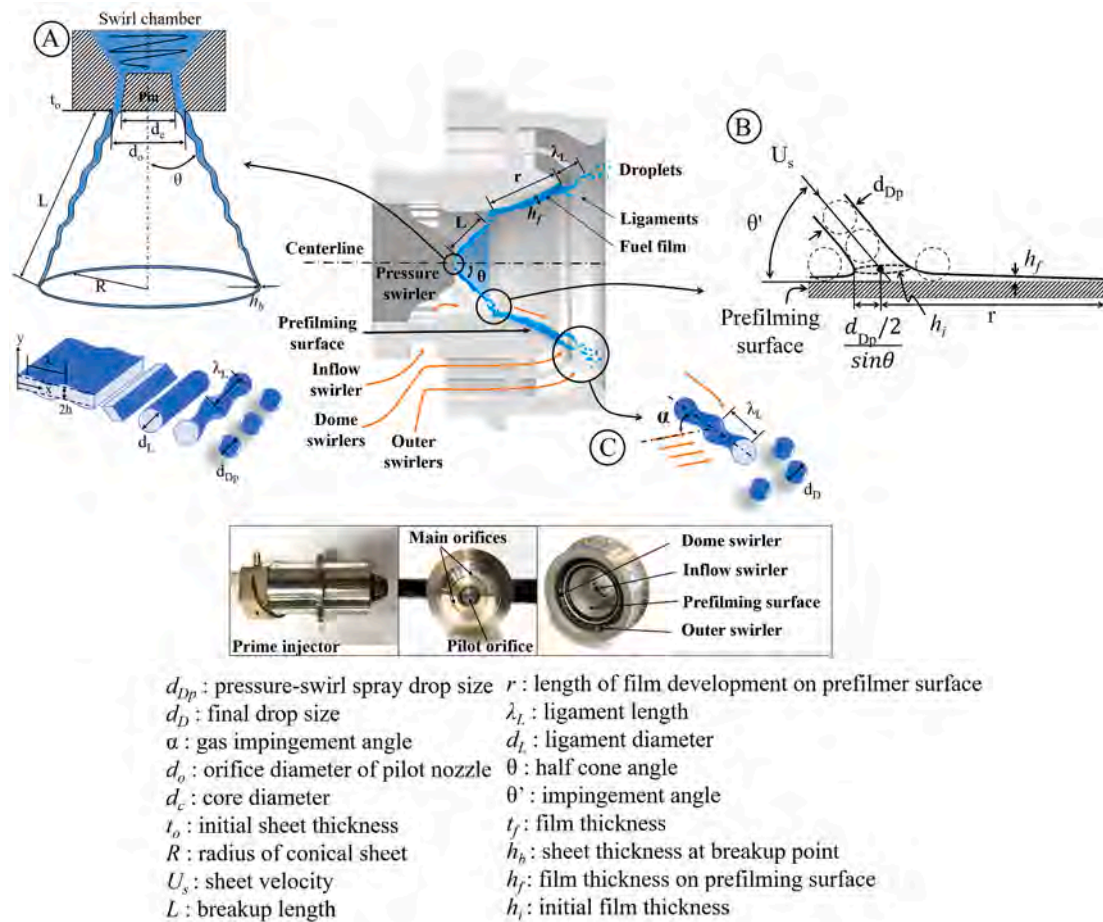


Fig. 14. Atomization process for the hybrid pressure-swirl airblast atomizer and photograph of the atomizer. Note that this diagram is adapted from work by Shin et al. [21].

gas stream increases. This causes the atomizing gas to transfer a fraction of its kinetic energy to the surrounding gas instead of the liquid [53]. Moreover, the interference between the atomizing gas streams from the dome and outer swirlers increases as the radial expansion increases at higher ALR ; thereby, the fraction of the atomizing energy will be reduced. The values for constants a' , b' , and c' in the parameter C were iterated for the best agreement with the experimental data and were determined to be 3.0, 0.2, and 1.65, respectively. These constants are not the same as ones from the previous study [21], but were adjusted to take all measurements at LBO [13], cold start [21], and high ambient pressure conditions into consideration in the model. The model predictions presented in the later section of this work were predicted using this adjusted parameter C and its constants.

Fig. 15 shows the predictions of essential parameters from each sub-model, such as the pressure-swirl spray drop size (d_{Dp}), fuel film thickness (t_f), and its flow velocity (U_{film}) on the prefilming surface, ligament diameter (d_L), and ligament length (λ_L). Except for the film velocity, these parameters were dimensionalized by the pilot nozzle orifice diameter (d_o). As shown in Fig. 15(a), the droplet diameter of the pressure-swirl spray was predicted to decrease with increasing ambient pressure [2,24,46]. This is due to a greater gas inertial force by increasing gas density. The gas flow with a greater inertial force causes the growth rate and wavenumber of disturbance on the liquid sheet (pressure-swirl spray) to increase. This resulted in a smaller droplet diameter from the sheet/ligament breakup of the pressure-swirl spray. Due to the smaller droplet size predicted at higher ambient pressure, the film thickness formed on the prefilmer surface was predicted to become

thinner as the ambient pressure increases, as shown in Fig. 15(b). Based on the continuity, the film flow velocity was predicted to be increased as the film gets thinner since the fuel mass flow rate was set to be constant.

The ligament diameter and length were predicted to decrease with increasing ambient pressure, as shown in Fig. 15 (c) and (d). The ligament diameter is a function of film thickness and wavenumber of the film. At higher ambient pressure, the wavenumber of the film increases as the growth rate of disturbance on the film rises due to a higher density of gas flowing along with the film. Hence, the ligament diameter was predicted to decrease with increasing ambient pressure. Similarly, a higher growth rate of disturbance on the ligament with a higher wavenumber of the ligament caused the ligament length to be decreased with increasing ambient pressure.

The comparisons of dimensionless predicted (d_D/d_o) and measured drop sizes (D_{320}/d_o) for A-2 and C-5 fuels are shown in Fig. 16 for $\Delta P/P = 3\%$, $\Delta P_{pilot} = 1.72$ bar, $T_{fuel} = 332$ K, $T_{airbox} = 394$ K, and $z = 25.4$ mm. The orifice diameter of the pilot nozzle (d_o) was used for this dimensionless quantity. The diminishing effect of ambient pressures on the drop size was observed for both A-2 and C-5 fuels. Moreover, it can be observed that the A-2 drop size are slightly larger than for C-5 fuel. The percentage difference in dimensionless measured drop sizes (D_{320}/d_o) between A-2 and C-5 fuels was 1% at $P_{vessel} = 1$ bar and 17% at $P_{vessel} = 9.5$ bar. This difference is believed to be due to the higher viscosity and surface tension of A-2 fuel compared to those of C-5 fuel, as shown in Table 4. Higher liquid viscosity and higher surface tension hinder bulk liquid deformation and disintegration through dissipation of the aerodynamic force by increasing the restorative force of the liquid and

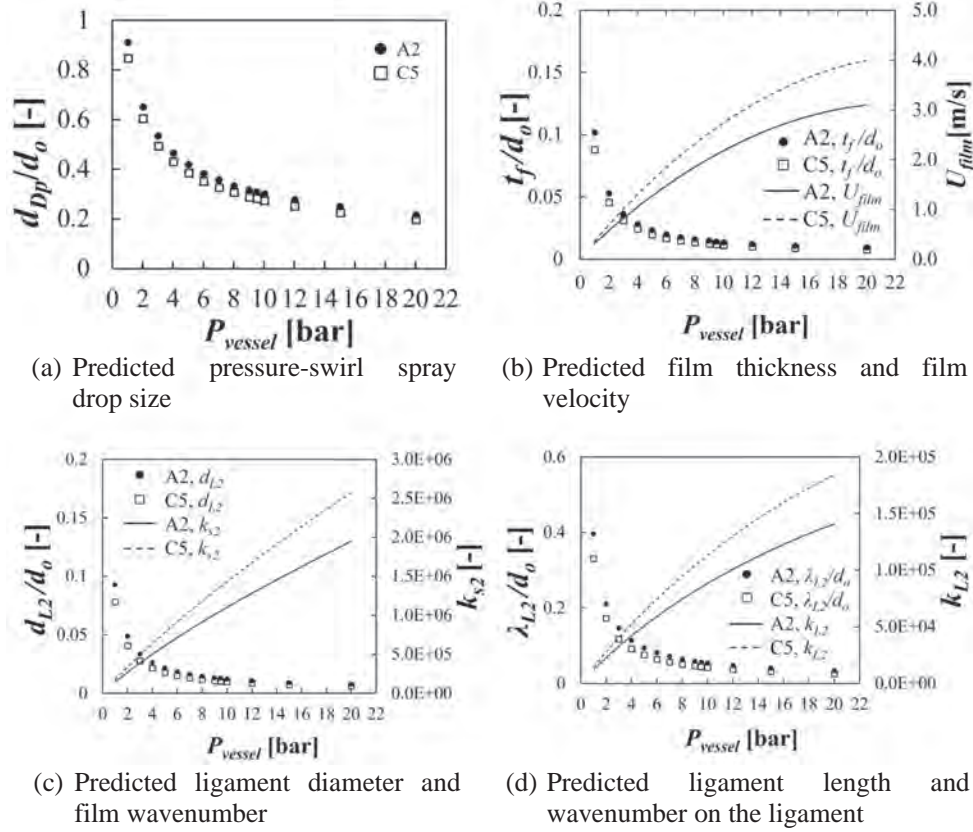


Fig. 15. Predictions for the pressure-swirl spray drop size (d_{pp}), film thickness on the prefilmer surface (t_f), film velocity (U_{film}), and ligament diameter (d_L), film wavenumber (k_{L2}), ligament length (λ_L), and ligament wavenumber (k_{L2}). The model predicted these parameters at $\Delta P/P = 3\%$, $\Delta P_{pilot} = 1.72$ bar, $T_{fuel} = 332$ K, and $T_{airbox} = 394$ K.

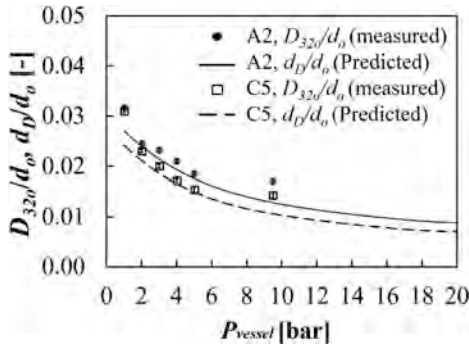


Fig. 16. Comparison of non-dimensionalized measured average drop sizes (D_{320}/d_o) and predicted drop size (d_p/d_o) at different ambient pressures for A-2 and C-5 fuels at $\Delta P/P = 3\%$, $\Delta P_{pilot} = 1.72$ bar, $T_{fuel} = 332$ K, and $T_{airbox} = 394$ K for $z = 25.4$ mm.

viscous damping effects [2,54]. This resulted in larger droplets for the A-2 fuel.

The model predicted drop sizes at $P_{vessel} = 1, 2, 3, 4,$ and 5 bar within $\pm 6\%$ and drop sizes at $P_{vessel} = 9.5$ bar with approximately 17% error compared to experimental data. This inaccuracy in the drop size prediction is believed to be due to the assumptions and simplifications in each sub-model, such as the inviscid assumptions for the cone angle estimation, film thickness estimation on the prefilmer surface, simplified drop-surface interaction mechanisms, etc [13]. For accurate predictions, a viscous film formation analysis including all droplet-surface interaction mechanisms such as droplet stick, spread, splash, and droplet rebound in the drop impingement and film formation sub-model would

likely be necessary. Therefore, more experimental work such as X-ray measurements within the atomizer would provide additional insights into the drop formation at high ambient pressure and would also help to validate our proposed model experimentally. The uncertainty bars for D_{320} were obtained by applying the same weight factor that was used for D_{320} to each uncertainty (standard deviation) of measured D_{32} at each radial location. The uncertainty values were observed to be within 3% for both A-2 and C-5 fuels.

Fig. 17 shows the comparison of predicted and measured dimensionless drop sizes for A-2 fuel at $\Delta P/P = 2, 3,$ and 6% , $P_{vessel} = 5$ bar, $\Delta P_{pilot} = 1.72$ bar, $T_{fuel} = 332$ K, and $T_{airbox} = 394$ K for $z = 25.4$ mm. The model predicted the drop size at different $\Delta P/P$ within 17% error and successfully demonstrated the drop size trend observed with $\Delta P/P$ variation at $P_{vessel} = 5$ bar. The uncertainty bars for D_{320} in Fig. 17 were

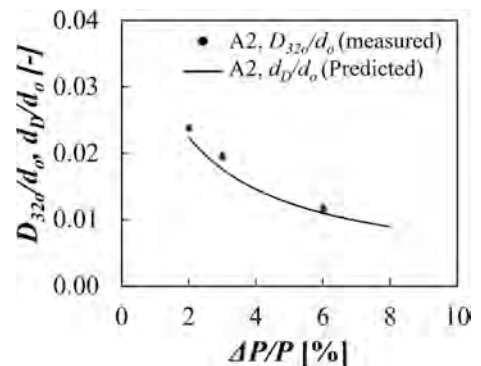


Fig. 17. Comparison between the measured and predicted dimensionless drop sizes at $\Delta P/P = 2, 3,$ and 6% and $P_{vessel} = 5$ bar for A-2 fuel.

also obtained in the same way for those in Fig. 16, and the uncertainty were observed to be within 5%.

6. Conclusions

The characteristics of a non-reacting spray, generated by the hybrid pressure-swirl airblast (HPSA) atomizer, were investigated under high ambient pressure conditions for a standard and an alternative aviation fuel using PDA and simultaneous PLIF and Mie imaging techniques.

A significant reduction in D_{32} was observed with increasing P_{vessel} from 1 bar to 9.5 bar. This is attributed to higher ambient gas density causing a greater drag force and greater inertial force on the bulk of liquid resulting in smaller droplets. However, the effect of ambient pressure on the drop size diminished with a further increase in ambient pressure. Furthermore, the spray tends to have a monodisperse droplet at higher ambient pressure. The droplet sizes of A-2 fuel were greater than those for C-5 fuel due to the higher viscosity and surface tension of the A-2 fuel. The axial drop velocity was observed to be similar for all ambient pressures, but droplets near the spray edge were observed to slow down with increasing pressure. A larger number of smaller droplets were observed at higher ambient pressures. The Mie scattering data indicate that these droplets tended to recirculate into the hollow-cone region. Moreover, the smaller droplets near the spray edge tended to follow the gas flow. The spray cone angles at $z = 6.0$ and 25.4 mm were observed to be independent of ambient pressure for both A-2 and C-5 fuels. However, the spray cone angle at $z = 18$ mm was observed to increase with increasing ambient pressure due to the entrainment of smaller droplets at higher ambient pressure. The LSD technique with the conventional fuel-PLIF and Mie scattering images was limited for the spray at variable ambient pressure conditions due to the high concentration of the aromatic contents in the fuel and multiple scattering. Hence, SLIPI with an appropriate concentration of the fluorescent dye was suggested.

A phenomenological three-step atomization model, including pressure-swirl spray droplet formation, droplet impingement and film formation, and aerodynamic breakup, provided some valuable insights into the effect of the ambient pressure on the drop formation as it successfully demonstrated the drop size trend with increasing ambient pressure. The model predicted the drop size within ± 6 for $P_{vessel} = 1, 2, 3, 4,$ and 5 bar cases and 17% for $P_{vessel} = 9.5$ bar. This is believed to be due to the assumptions and simplifications in the analysis. Further experimental work, such as X-ray measurements within the HPSA atomizer, would provide additional insights into the spray morphology and be helpful to validate the model further.

Funding

This research was funded by the U.S. Federal Aviation Administration Office of Environment and Energy through ASCENT, the FAA Center of Excellence for Alternative Jet Fuels and the Environment, Project 29A through FAA Award Number 13-C-AJFE-PU-011 under the supervision of Dr. Cecilia Shaw and Dr. Anna Oldani. Any opinions, findings, conclusions or recommendations expressed in this material are those of the authors and do not necessarily reflect the views of the FAA.

CRedit authorship contribution statement

Dongyun Shin: Conceptualization, Methodology, Formal analysis, Investigation, Writing – original draft. **Aman Satija:** Investigation, Writing – review & editing. **Robert P. Lucht:** Supervision, Writing – review & editing.

Declaration of Competing Interest

The authors declare that they have no known competing financial interests or personal relationships that could have appeared to influence

the work reported in this paper.

Acknowledgment

The authors thank Dr. Tim Edwards at the Air Force Research Laboratory for providing the fuels and information about their physical properties.

References

- [1] M. Colket, J. Heyne, M. Rumizen, M. Gupta, T. Edwards, W.M. Roquemore, G. Andac, R. Boehm, J. Lovett, R. Williams, J. Condevaux, D. Turner, N. Rizk, J. Tishkoff, C. Li, J. Moder, D. Friend, V. Sankaran, Overview of the National Jet Fuels Combustion Program, *AIAA J.* 55 (4) (2017) 1087–1104, <https://doi.org/10.2514/1.J055361>.
- [2] A.H. Lefebvre, V.G. McDonell, "Atomization and Sprays," Hemisphere Publishing Corporation, 1989.
- [3] M.P. Boyce, "Gas Turbine Engineering Handbook", Butterworth-Heinemann, 4th ed., 2011.
- [4] I.V. Roisman, C. Tropea, F.Z. Batarseh, Characterization of a Spray Generated by an Airblast Atomizer with Prefilmer, *Atomization Sprays* 20 (10) (2010) 887–903, <https://doi.org/10.1615/AtomizSpr.v20.i10.50>.
- [5] J. Becker, C. Hassa, Experimental Investigation of Spatial and Temporal Aspects of the Liquid Fuel Placement in a Swirl Cup at Elevated Pressure, "ASME Turbo Expo 2004: Power for Land, Sea, and Air, Vol. 1, No. GT2004-53524, June. 14-17, pp. 351-360, 2004. 10.1115/GT2004-53524.
- [6] M. Chrigui, I.V. Roisman, F.Z. Batarseh, A. Sadiki, C. Tropea, Spray Generated by an Airblast Atomizer Under Elevated Ambient Pressures, *J. Propul. Power* 26 (6) (2010) 1170–1183, <https://doi.org/10.2514/1.47833>.
- [7] A. Corber, N. Rizk, W.A. Chishty, Experimental and Analytical Characterization of Alternative Aviation Fuel Sprays under Realistic Operating Conditions, *J. Eng. Gas Turbines Power* 141 (6) (2019), 061022, <https://doi.org/10.1115/1.4041649>.
- [8] G. Chaussonnet, S. Geppert, S. Holz, R. Koch, H.J. Bauer, Influence of the ambient pressure on the liquid accumulation and on the primary spray in prefilming airblast atomization, *Int. J. Multiph. Flow* 125 (2020) 103229, <https://doi.org/10.1016/j.ijmultiphaseflow.2020.103229>.
- [9] A.K. Jasuja, Airblast Atomization of Alternative Liquid Petroleum Fuels under High Pressure Conditions, *ASME J. Eng. Power* 103 (3) (1981) 514–518, <https://doi.org/10.1115/1.3230751>.
- [10] Q.P. Zheng, A.K. Jasuja, A.H. Lefebvre, Structure of airblast sprays under high ambient pressure conditions, "ASME Turbo Expo 1996: Power for Land, Sea, and Air, Vol. 3, No. 96-GT-131, pp. V003T06A022, 1996. 10.1115/96-GT-131.
- [11] R.K. Hanson, J.M. Seitzman, P.H. Paul, Planar Laser-Fluorescence Imaging of Combustion Gases, *Appl. Phys. B* 50 (6) (1990) 441–454, <https://doi.org/10.1007/BF00408770>.
- [12] T.D. Fansler, D.L. Reuss, V. Sick, R.N. Dahms, "Invited Review: Combustion Instability in Spray-Guided Stratified-Charge Engines: A review, *Int. J. Engine Res.* 16 (3) (2015) 260–305, <https://doi.org/10.1177/1468087414565675>.
- [13] D. Shin, A.J. Bokhart, N.S. Rodrigues, P.E. Sojka, J.P. Gore, R.P. Lucht, Non-Reacting Spray Characteristics for Alternative Aviation Fuels at Near Lean Blowout Conditions, *J. Propulsion Power* 36 (3) (2020) 323–334, <https://doi.org/10.2514/1.B37712>.
- [14] B. Sforzo, A.L. Kastengren, K.E. Matusik, F.G. del Campo, C.F. Powell, X-Ray Phase Contrast Imaging of Liquid Film and Spray Development Inside an Aircraft Engine Swirler, *J. Eng. Gas Turbines Power*, 141(12), GT2019-1387, 2019. 10.1115/1.4045217.
- [15] A. Mansour, M. Benjamin, T. Burke, A. Odar, B. Savel, "Hybrid Atomizing Fuel Nozzle," U.S. Patent 6547163 B1, 2003.
- [16] M. Orain, P. Baranger, C. Ledier, J. Apeloig, F. Grisch, Fluorescence Spectroscopy of Kerosene Vapour at High Temperatures and Pressures: Potential for Gas Turbines Measurements, *Appl. Phys. B* 116 (3) (2014) 729–745, <https://doi.org/10.1007/s00340-013-5756-z>.
- [17] M. Suto, X. Wang, J. Shan, L.C. Lee, Quantitative Photoabsorption and Fluorescence Spectroscopy of Benzene, Naphthalene, and Some Derivatives at 106–295 nm, *J. Quant. Spectrosc. Radiat. Transfer* 48 (1) (1992) 79–89, [https://doi.org/10.1016/0022-4073\(92\)90008-R](https://doi.org/10.1016/0022-4073(92)90008-R).
- [18] M. Ordain, P. Baranger, B. Rossow, F. Grisch, Fluorescence Spectroscopy of 1,2,4-trimethylbenzene at High Temperatures and Pressures: Application to Temperature Measurements, *Appl. Phys. B* 100 (2010) 945–952, <https://doi.org/10.1007/s00340-010-3967-0>.
- [19] T. Edwards, Reference Jet Fuels for Combustion Testing, *AIAA Paper* 2017–0146 (2017), <https://doi.org/10.2514/6.2017-0146>.
- [20] H.E. Albrecht, M. Borys, N. Damaschke, C. Tropea, "Laser Doppler and Phase Doppler Measurement Techniques," Springer-Verlag Berlin Heidelberg, pp. 169–523, 2003. 10.1007/978-3-662-05165-8.
- [21] D. Shin, N.S. Rodrigues, A.J. Bokhart, P. Sojka, J.P. Gore, R.P. Lucht, Spray Characteristics of Standard and Alternative Aviation Fuels at Cold Start Conditions, *AIAA Journal* 2021, in press.
- [22] L.G. Dodge, D.J. Rhodes, R.D. Reitz, Drop-Size Measurement Techniques for Sprays: Comparison of Malvern Laser-Diffraction and Aerometrics phase/Doppler, *Appl. Opt.* 26 (11) (1987) 2144–2154, <https://doi.org/10.1364/ao.26.002144>.
- [23] S.J. Kline, F.A. McClintock, Describing Uncertainties in Single Sample Experiments, *Mech. Eng.* 75 (1) (1953) 3–8, <https://doi.org/10.1007/s00348-015-1917-7>.

- [24] S.M. DeCorso, Effect of Ambient and Fuel Pressure on Spray Drop Size, *J. Eng. Power* 82 (1) (1960) 10–18.
- [25] G. Charalampous, Y. Hardalupas, Method to Reduce Errors of Droplet Sizing based on the Ratio of Fluorescent and Scattered Light Intensities (laser-induced fluorescence/Mie technique), *OSA Appl. Optics* 50 (20) (2011) 3622–3637, <https://doi.org/10.1364/AO.50.003622>.
- [26] P. Le Gal, N. Farrugia, D.A. Greenhalgh, Laser Sheet Dropsizing of Dense Sprays, *Optics Laser Technol.* 31 (1) (1999) 75–83, [https://doi.org/10.1016/S0030-3992\(99\)00024-9](https://doi.org/10.1016/S0030-3992(99)00024-9).
- [27] S.V. Sankar, K.E. Maher, D.M. Robart, W.D. Bachalo, 1999, "Rapid Characterization of Fuel Atomizers Using an Optical Patternator.", *ASME. J. Eng. Gas Turbines Power.* 121 (3) (July 1999) 409–414, <https://doi.org/10.1115/1.2818488>.
- [28] C.N. Yeh, H. Kosaka, T. Kamimoto, A Fluorescence/Scattering Imaging Technique for Instantaneous 2-D Measurements of Particle Size Distribution in a Transient Spray, in: *Proc, 3rd Congr., on Opt, Part. Sizing, Yokohama, Japan, 1993*, pp. 355–361.
- [29] M.C. Jermy, D.A. Greenhalgh, Planar Dropsizing by Elastic and Fluorescence Scattering in Sprays Too Dense for Phase Doppler Measurement, *Appl Phys B* 71 (5) (2000) 703–710, <https://doi.org/10.1007/s003400000404>.
- [30] A.P. Kulkarni, V.D. Chaudhari, S.R. Bhadange, D. Deshmukh, Planar Drop-Sizing and Liquid Volume Fraction Measurements of Airblast Spray in Cross-Flow Using SLIPI-based Techniques, *Int. J. Heat Fluid Flow* 80 (2019) 108501, <https://doi.org/10.1016/j.ijheatfluidflow.2019.108501>.
- [31] K. Kannaiyan, M.V.K. Banda, A. Vaidyanathan, Planar Sauter Mean Diameter measurements in Liquid centered Swirl Coaxial Injector Using Laser Induced Fluorescence, Mie scattering and Laser Diffraction Techniques, *Acta Astronautica* 123 (2016) 257–270, <https://doi.org/10.1016/j.actaastro.2016.03.011>.
- [32] Y.N. Mishra, E. Kristensson, E. Berrocal, Reliable LIF/Mie Droplet Sizing in Sprays using Structured Laser Illumination Planar Imaging, *Optical Soc. Am.* 22 (4) (2014) 4480, <https://doi.org/10.1364/OE.22.004480>.
- [33] Y.N. Mishra, E. Kristensson, M. Koegl, J. Jönsson, L. Zigan, E. Berrocal, Comparison between Two-Phase and One-Phase SLIPI for Instantaneous Imaging of Transient Sprays, *Exp. Fluids* 58 (9) (2017), <https://doi.org/10.1007/s00348-017-2396-9>.
- [34] B.D. Stojkovic, V. Sick, Evolution and Impingement of an Automotive Fuel Spray Investigated with Simultaneous Mie/LIF Techniques, *Appl. Phys. B* 73 (1) (2001) 75–83, <https://doi.org/10.1007/s003400100598>.
- [35] E. Berrocal, E. Kristensson, M. Richter, M. Linne, M. Aldén, Application of Structured Illumination for Multiple Scattering Suppression in Planar Laser Imaging of Dense Sprays, *Opt. Express* 16 (22) (2008) 17870–17881, <https://doi.org/10.1364/OE.16.017870>.
- [36] J.W. Powell, C.F. Lee, An Investigation of Multiple Scattering in a Hollow-Cone Spray, *SAE Paper* 2007-01-0648, 2007, 10.4271/2007-01-0648.
- [37] R. Domann, Y. Hardalupas, A Study of Parameters that Influence the Accuracy of the Planar Droplet Sizing (PDS) Technique, *Part. Part. Syst. Char.* 18 (1) (2001) 3–11, [https://doi.org/10.1002/1521-4117\(200102\)18:1<>1.0.CO;2-#10.1002/1521-4117\(200102\)18:1<3::AID-PPSC3>3.0.CO;2-#](https://doi.org/10.1002/1521-4117(200102)18:1<>1.0.CO;2-#10.1002/1521-4117(200102)18:1<3::AID-PPSC3>3.0.CO;2-#).
- [38] J.V. Pastor, J.J. Lopez, J.E. Juliá, J.V. Benajes, Planar Laser-Induced Fluorescence Fuel Concentration Measurements in Isothermal Diesel Sprays, *Opt. Express* 10 (7) (2002) 309–323, <https://doi.org/10.1364/OE.10.000309>.
- [39] Richard Viskup, 2020, *Diesel and Gasoline Engines*, IntechOpen, Chap.5. ISBN: 978-1-78985-447-3, 10.5772/intechopen.75259.
- [40] R. Domann, Y. Hardalupas, Quantitative Measurement of Planar Droplet Sauter Mean Diameter in Sprays using Planar Droplet Sizing, *Part. Part. Syst. Char.* 20 (3) (2003) 209–218, <https://doi.org/10.1002/ppsc.v20:310.1002/ppsc.200390027>.
- [41] G. Laufer, Properties of Electromagnetic Waves. In *Introduction to Optics and Lasers in Engineering*, Cambridge: Cambridge University Press., pp.87–121, 1996. 10.1017/CBO9781139174190.006.
- [42] J. Canny, A Computational Approach to Edge Detection, in: *IEEE Transactions on Pattern Analysis and Machine Intelligence*, Vol.PAMI-8, No.6, pp.679–698, 1986, 10.1109/TPAMI.1986.4767851.
- [43] M. Zaller, R.J. Locke, R.C. Anderson, Comparison of Techniques For Non-Intrusive Fuel Drop Size Measurements in a Subscale Gas Turbine Combustor, *J. Vis.* 2 (2000) 301–308, <https://doi.org/10.1007/BF03181446>.
- [44] M. Linne, Imaging in the Optically Dense Regions of a Spray: A Review of Developing Techniques, *Prog. Energy Combust. Sci.* 39 (5) (2013) 403–440, <https://doi.org/10.1016/j.pecs.2013.06.001>.
- [45] J. Zelina, A. Rodrigue, Fuel Injector Characterization using Laser Diagnostics at Atmospheric and Elevated Pressures, *AIAA-98-0148*, 1998. 10.2514/6.1998-148.
- [46] X.F. Wang, A.H. Lefebvre, Influence of Ambient Air Pressure on Pressure-Swirl Atomization, in: *Proceedings of the ASME 1987 International Gas Turbine Conference and Exhibition, 3: Coal, Biomass and Alternative Fuels; Combustion and Fuels; Oil and Gas Applications; Cycle Innovations*. Anaheim, California, USA. May 31–June 4, 1987. V003T06A003, 1987. ASME. 10.1115/87-GT-55.
- [47] L.G. Dodge, J.A. Biaglow, Effect of Elevated Temperature and Pressure on Sprays From Simplex Swirl Atomizers, *ASME. J. Eng. Gas Turbines Power.* 108 (1) (1986) 209–215, <https://doi.org/10.1115/1.3239873>.
- [48] P.K. Senecal, D.P. Schmidt, I. Nouar, C.J. Rutland, R.D. Reitz, M.L. Corradini, Modeling High Speed Viscous Liquid Sheet Atomization, *Int. J. Multiph. Flow* 25 (6–7) (1999) 1073–1097, [https://doi.org/10.1016/S0301-9322\(99\)00057-9](https://doi.org/10.1016/S0301-9322(99)00057-9).
- [49] J.D. Naber, R.D. Reitz, Modeling Engine Spray/Wall Impingement, *J. Engines* 97 (6) (1988) 118–140. <https://www.jstor.org/stable/44547362>.
- [50] E.A. Ibrahim, A.J. Przekwas, Impinging Jets Atomization, *Phys. Fluids A Fluid Dyn.* 3 (12) (1991), <https://doi.org/10.1063/1.857840>.
- [51] A.H. Lefebvre, Energy Considerations in Twin Fluid Atomization, *J. Eng. Gas Turbines Power* 114 (1) (1992) 89–96, <https://doi.org/10.1115/1.2906311>.
- [52] J.E. Beck, T.R. Lefebvre, Liquid Sheet Disintegration by Impinging Air Streams, *Atomization Sprays* 1 (2) (1991) 155–170, <https://doi.org/10.1615/AtomizSpr.v1.i2.20>.
- [53] P.E. Sojka, K.E. Knoll, Flat-Sheet Twin-Fluid Atomization of High Viscosity Fluids. Part I: Newtonian Liquids, *Atomization Sprays* 2 (1) (1992) 17–36, <https://doi.org/10.1615/AtomizSpr.v2.i1.20>.
- [54] A.A. Rizkalla, A.H. Lefebvre, Influence of Liquid Properties on Airblast Atomizer Spray Characteristics, *J. Eng. Power Am. Soc. Mech. Eng.* 97 (2) (1975) 173–177, <https://doi.org/10.1115/1.3445951>.